J. Min. Metall. Sect. B-Metall. 59 (1) (2023) 169 - 182

Journal of Mining and Metallurgy, Section B: Metallurgy

MICROSTRUCTURE DEVELOPMENT, MECHANICAL PROPERTIES AND UNDERLYING MECHANISM OF MICRO-TiN-REINFORCED AlSi10Mg COMPOSITES FABRICATED BY SELECTIVE LASER MELTING

X. Huang [a, b], L. Wang [b], W.-D. Huang [a, b, *], D.-D. He [b], X.-H. Cheng [b], X.-P. Xu [b], X.-X. Chen [b], S.-S Qin [a, b], L.-H. Huang [a, b]

[a] Fujian Key Laboratory of Intelligent Machining Technology and Equipment, Fujian University of Technology, Fuzhou, China

[b] School of Mechanical and Automotive Engineering, Fujian University of Technology, Fuzhou, China

(Received 12 January 2023; Accepted 22 May 2023)

Abstract

In this study, aluminum matrix composites reinforced with micro-TiN were fabricated using selective laser melting (SLM) technique. The study investigates the effects of TiN content on densification, microstructure evolution, crystal textures, and mechanical properties. The results show that the relative density of composite samples containing 0–3 wt. % TiN exceeds 98%. However, further increase in TiN content leads to a decrease in relative density. The TiN particles are uniformly distributed and wetted by the AlSi10Mg matrix, forming a graded interfacial layer. The TiN particles refine the matrix grains and significantly reduce the prevalence (001) texture by promoting a heterogeneous nucleation process. In comparison to the AlSi10Mg alloy, the TiN/AlSi10Mg composite exhibits improved microhardness, tensile strength, and wear resistance. The exceptional mechanical properties of the Al matrix composites are attributed to the dispersion strengthening of the TiN particles and the fine-grain strengthening of the matrix. The optimal TiN content is found to be 3 wt. %, resulting in excellent mechanical performance of the fabricated samples (132.4±4.1 HV for hardness and 379.7±4.6 MPa for tensile strength) with a low friction coefficient of 0.49.

Keywords: *Selective laser melting; TiN/AlSi10Mg composites; Microstructure development; Mechanical properties*

1. Introduction

Aluminum alloy is the second most prevalent metal structural material after steel. It is characterized by low density, high specific strength, excellent electrical conductivity, and can be used in the biomedical application after anodizing. By introducing reinforcement, its strength, heat resistance and wear resistance can be further improved [1, 2]. Traditional preparation methods of aluminum alloy and aluminum matrix composites (AMCs) include casting, forging and powder metallurgy, which have problems such as long manufacturing cycles, high mold costs, difficulty in forming complex geometric components and material waste [3]. Selective laser melting (SLM) is a new and advanced additive manufacturing technology with a unique layered processing method that facilitates the formation of solid parts with complex structures, realizes the new material processing concept of "near net forming", improves cost-effectiveness, and achieves a high performance that is difficult to achieve with traditional preparation processes [4, 5]. The literature highlights that selective laser melted particle-reinforced aluminum matrix composites (PRAMCs) have many advantages.

The first is the second-phase strengthening caused by ceramic particles and the grain refinement during the SLM process. The reinforcements of AMCs are generally hard particles, such as SiC, Al_2O_3, TiN, TiB_2, ZrO_2, SiO_2, and other ceramic particles. These reinforced particles have a high melting point, hardness, strength, and elastic modulus. Adding them into an aluminum matrix can not only improve the strength, hardness and wear resistance of the resulting composite materials but also provide nucleation sites for grain refinement [6, 7]. The rapid cooling rate (up to 10^6 K/s) during the formation process leads to a large temperature gradient, resulting in the Marangoni effect, which causes a thermal capillary force of the liquid, which in turn acts on the reinforced particles in the molten pool, resulting in the dispersion strengthening of the reinforced phase. Wang [8] used the ball milling method to homogeneously mix

Corresponding author: hwd@fjut.edu.cn

https://doi.org/10.2298/JMMB230112015H

AlSi7Mg alloy powder with nano-SiC particles. During the SLM process, Al and SiC underwent a chemical reaction to form a hard nano-Al_4C_3 phase. Due to the solution strengthening, fine-grain strengthening and precipitation strengthening of the Si, Mg_2Si and Al_4C_3 phases, the tensile strength reached 503 MPa.

In the SLM process, the characteristics of a low laser absorption and high thermal conductivity of aluminum alloy seriously affect its formability. The addition of ceramic particles helps to increase the laser absorption rate of the composite and thus improves its forming quality. The laser absorptivity (A) of the composite powder can be calculated by the formula

$$A = A_1\gamma_1 + A_2\gamma_2$$

(A_i and γ_i are the laser absorptivity and volume fraction of the corresponding powder) [9]. Ceramics, such as TiB_2, B_4C, SiC, TiN, and TiC, have higher A values than aluminum alloy powders under 1070 nm wavelength lasers. The introduction of ceramic particles into aluminum alloy powder can improve its high reflectivity. Gao [10] modified the surface of AlSi10Mg powder by adding nano-TiN particles to form alloy samples with a density of 97.6% at a low laser power of 100 W. Li [11] used a 7 vol% nano-TiB_2 coating on the surface of AlSi10Mg powder, which increased the laser absorption rate of AlSi10Mg powder from 63% to 71%.

Regarding hard particles, TiN particles have a good thermal stability (melting point up to 2930 °C), high hardness and high wear resistance [12], which is particularly suitable for the strengthening phase. The laser absorption rates of TiN and AlSi10Mg at a 1070 nm wavelength are 0.78 and 0.48, respectively, and the addition of TiN can improve the laser absorptivity of AlSi10Mg powder. In previous works, the laser reflectivity and process parameters of this composite were studied. Therefore, on the basis of previous research, the effects of the TiN content on the densification behavior, microstructure evolution, crystal textures and mechanical properties of the SLM samples are investigated, as well as the mechanism underlying the improvements in strength, ductility and wear resistance.

2. Methods and experiments

2.1. Materials and SLM process

The starting materials used in this experiment were TiN particles (1-4.4 μm, Aladdin, Shanghai) and

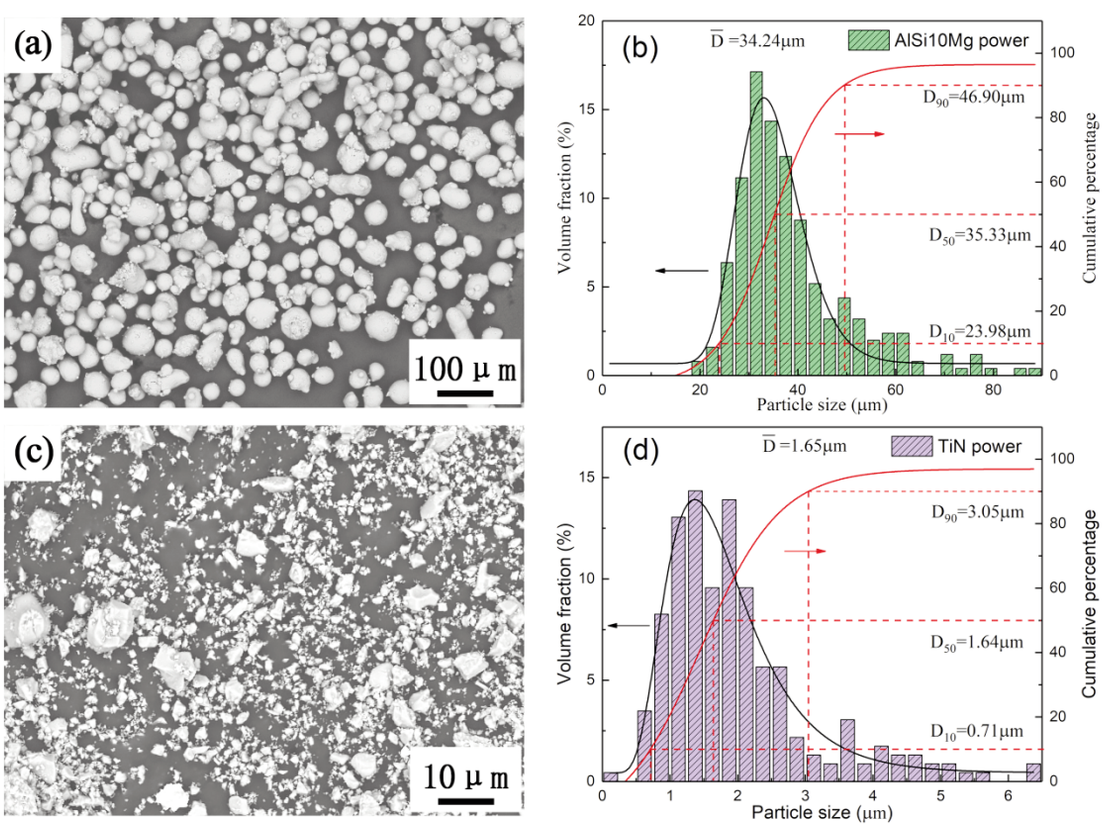

Figure 1. *Morphologies of the original powders and their particle size distributions: (a)(b) AlSi10Mg and (c)(d) TiN*

AlSi10Mg powder (20-63 μm, Bedorno, Chengdu). The AlSi10Mg powder had a nearly spherical shape (Fig. 1 (a)) with an average particle size of 34.24 μm (Fig. 1 (b)), and its chemical composition is listed in Table 1. The micro-TiN particles were irregular (Fig. 1 (c)), and the average particle size was approximately 1.65 mm (Fig. 1 (d)). TiN/AlSi10Mg composite powders with different TiN contents (0, 1, 3 and 5 wt.%) were designed and mechanically ball milled for 4 hours in an argon atmosphere. The TiN/AlSi10Mg composite was fabricated using a SLM solution 125 HL device, and the specimens were labeled as S0, S1, S3, and S5. Before the experiment, the SLM processing parameters were determined as follows: a laser power of 350 W, a scanning speed of 1650 mm/s, a hatching distance of 0.13 mm, and a layer thickness of 0.03 mm. An argon atmosphere (O2<1000 ppm) was applied to avoid oxidation of the fabricated samples with a substrate preheating temperature of 100 °C. In addition, a linear scanning strategy with an interlaminar scanning deflection angle of 67° was used.

Table 1. *Chemical compositions of AlSi10Mg powder*

Element	Al	Si	Cu	Mn	Mg	Zn	Ti	Fe
Mass fraction (%)	Bal.	11	0.3	0.03	0.4	0.3	0.1	0.15

2.2. Characterization

The size of the square specimen formed by SLM was 10 mm×10 mm. After grinding with sandpaper, the weight of the samples was measured by an ME204E analytical balance (Zurich, Switzerland). The real density of the sample was determined by the Archimedes drainage method. The relative density is the ratio of the real density to the theoretical density. The phase detection of the composite powder and SLM samples was conducted by X-ray diffraction (XRD, D8ADVANCE, Billerica, USA) with a fast scan of 4°/min over a (2θ) 20–80° scanning range using a Cu-Ka radiation source at 40 V and 40 mA. After rough grinding and fine polishing, the samples were etched for 15 s with Keller reagent (1 vol% HF +1.5 vol% HCl+2.5 vol% HNO_3+95 vol% H_2O) and then cleaned by ultrasonication for 15 min before vacuum drying. Then, the microstructure was observed using an optical microscope (OM, KH1300, Tokyo, Japan) and a field-emission scanning electron microscope (SEM, NovaNanoSEM450, Hillsboro, USA) equipped with an energy dispersion spectrum (EDS). Electron backscattered diffraction (EBSD) was used to analyze the grain size, grain orientation and texture of the samples. The samples were further electropolished in a solution comprising perchloric acid and ethanol in a volumetric ratio of 10:90 at -40 °C with an applied voltage of 12 V for 15 s. Wear tests were performed at room temperature using a tribometer (Bruker UMT-2 TriboLab, Billerica, USA). Si3N4 with a diameter of 10 mm was used in the test, and the linear reciprocating friction mode was adopted with a abrasion length of 4 mm, a load of 3 N and sliding time of 15 min. Microhardness was measured by a Vickers hardness tester (MVA-402TS, Shenzhen, China) with a load of 200 g and a duration time of 15 s. Eight points were measured for each sample, and the average value was regarded as the Vickers hardness. The as-built rectangular tensile specimens were tested at room temperature with a constant strain rate of 0.6 mm/min using a universal testing machine (INSTRON 2382, Boston, USA) according to the ASTM E8-04 standard. The cross-section size of the tensile specimens was 6 mm×2.5 mm with a standard distance of 20 mm. Three samples of each component material were tested, and the average value was taken as the final result.

3. Results

3.1. Densification behaviors

Fig. 2 shows the variation trend of the OM morphology and density of TiN/AlSi10Mg composites with different TiN contents. There are a few small pores in the S0 and S1 samples shown in Fig. 2(a-b), respectively. The formability of the composites deteriorates with increasing TiN addition. As shown in Fig. 2(c), the pore defects of the S3 sample are large spherical pores. Usually, smaller pores are formed by pores in the powder itself or by protective gases trapped in the molten pool. However, large pores are caused by excessive laser energy input and usually have high sphericity [13]. The Ramsay-Shields' equation defines the relationship between temperature and molten surface tension:

$$\gamma V_m^{2/3} = K(T_b - T - 6.0) \quad (1)$$

where γ is the surface tension, V_m is the molar volume, K is the universal constant, and T_b is the powder boiling temperature [14]. For the TiN/AlSi10Mg composites, due to the addition of TiN particles with a high laser absorptivity, the corresponding absorbed laser energy is greater. More energy input leads to a faster temperature rise, which leads to a greater recoil pressure [15]. According to Formula 1, the surface tension of the metal liquid decreases with increasing temperature, and the

elements (Al and Si) are more likely to evaporate from the molten pool, presenting large spherical defects. Sample S5 has irregular pores accompanied by a small number of cracks. Irregular pores are caused by molten solidification and fusion failure, and the cracks are mainly caused by residual stress. The thermal conductivity of AlSi10Mg (~108 $Wm^{-1}K^{-1}$) is much larger than that of TiN (~64 $Wm^{-1}K^{-1}$) [16]. Due to the difference in thermal conductivity between AlSi10Mg and TiN, the residual stress increases during thermal cycling. In addition, in the SLM process, melt cooling and shrinkage lead to tensile stress in solidification materials, and the temperature gradient mechanism (TGM) is an important reason for the formation of residual stress [17]. The relative densities of the SLM composites are shown in Fig. 2(e). With increasing TiN content, the relative density of the composites decreases gradually. When the TiN content is lower than 3 wt. %, the relative density of the sample is higher than 98%. Further increasing the TiN content results in a rapid decrease in the relative density of sample S5 to 96.47%.

makes the grains grow along the temperature gradient direction [19]. With the addition of TiN particles, the intensity of the Al (200) peak for samples S1, S3 and S5 decreases, while the intensity of the Al (111) peak increases. The preferred crystal orientation of the composites weakens. As the content of TiN particles increases, the intensity of the detected TiN peaks also increases gradually, suggesting that TiN promotes the transformation of crystal texture. In addition, due to lattice distortion caused by the addition of TiN particles and the increase in thermal stress caused by the high cooling rate, the diffraction peak corresponding to Al moves to a higher angle between 37.5-39.5° [20].

Fig. 4 shows the representative microstructures of the SLM samples in the x-y plane. The microstructures of specimens S0, S1, S3, and S5 exhibit a primary a-Al matrix decorated with brilliant white eutectic Si networks [21]. At the boundary of the molten pool (MP), due to the different thermal cycle histories, there are three different morphologies: MP fine, MP coarse and the heat affected zone (HAZ)

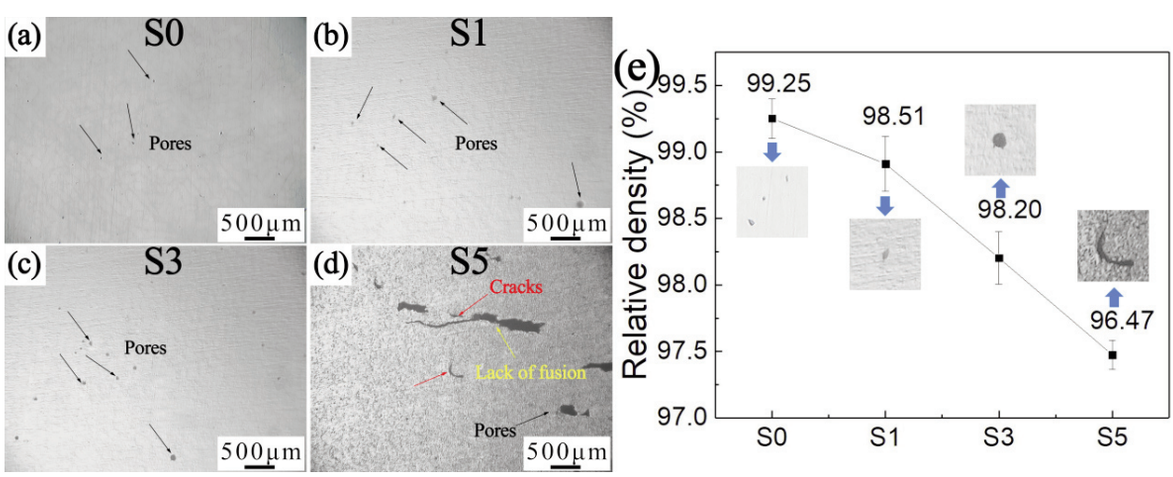

Figure 2. *(a)-(d) OM images and (e) relative densities of SLM samples with different additions of TiN*

3.2. Phase and microstructure analysis

Fig. 3 shows the XRD patterns of composite powders with different TiN contents and their corresponding SLM samples. Diffraction peaks of Al and Si are detected for all of the samples. Wide and weak Si peaks are observed for the SLM samples, indicating that a large amount of Si is supersaturated in the Al matrix. However, the peaks of Mg_2Si cannot be detected because the Mg content is lower than the detection limit [18]. For sample S0, the Al (200) peak is the strongest, while the Al (111) peak is weaker, indicating that a-Al preferentially solidifies along the <100> crystal direction, which is mainly attributed to the high heat gradient in the SLM process, which [22]. The microstructure of the sample is obviously refined when 1 wt.% TiN particles was added. However, due to the low TiN content, TiN particles are hardly observed in the Al matrix. When the TiN content is further increased to 3 wt. %, the fine microstructure remains and becomes more homogeneous. When the TiN content reaches 5 wt. %, the unmelted TiN particles in the aluminum matrix can be clearly observed, and some TiN particles are agglomerated and embedded in the matrix. The TiN particles that are not fully wetted with the matrix become the source of crack growth and reduce the density of the SLM TiN/AlSi10Mg composites. Compared to the network structure of samples S0-S3, the eutectic structure of sample S5 gradually changes

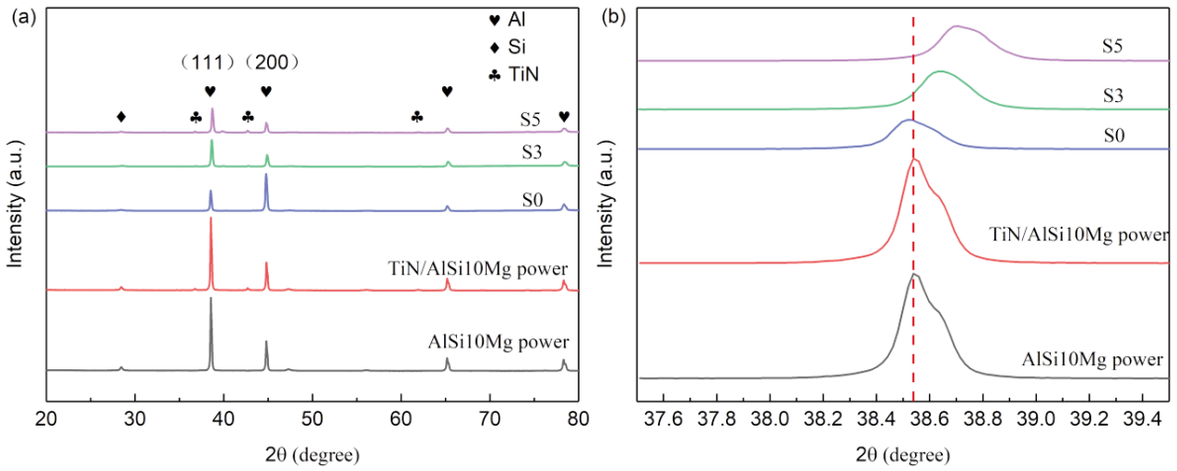

Figure 3. *XRD patterns of the composite powders and their corresponding SLM samples: (a) 2θ = 20~80° and (b) close-up view of 2θ = 38~39.5°*

from a network to thick sheets, part of the network structure is broken, and a large number of refined Si particles are dispersed in the a-Al matrix. The eutectic structure is mainly driven by the hydrodynamic force of the Marangoni flow, and the strong Marangoni flow caused by the higher temperature gradient promotes the continuous solidification of a-Al, resulting in a gradual increase in the concentration of Si in the residual liquid phase so that the liquid phase components gradually move toward the eutectic region to form an Al-Si eutectic structure. When too many TiN particles are added, the high melt viscosity and TiN agglomerates hinder Marangoni convection, resulting in poor melt fluidity, causing the eutectic structure to fracture and the cell structure to disappear [23].

As the melting point of TiN (2930 °C) is much higher than that of the Al matrix (1020 °C), the original TiN particles (Fig. 5(a)) are partially melted, and the irregular edges disappear during SLM processing. The dark region in the middle of the TiN particle is the unmelted part, and the surrounding light-colored annular area is the transition layer formed by the reaction between molten TiN and the Al matrix. The composition contents of Ti and N elements drop sharply in the transition layer, while the content of Al and Si increased.

3.3. Grain orientation and crystal textures

It can be seen from the XRD results above that the addition of TiN particles changes the intensity of the diffraction peak, so it is speculated that the preferred orientation of the crystal changes. Therefore, EBSD was used to study the grain orientation and crystal texture distribution of the AlSi10Mg and TiN/AlSi10Mg composites, and the results are shown in Fig. 5. Fig. 5(a) and (c) show the grain size distribution of samples S0 and S3. Among them, the S0 sample has a microstructure that is mainly composed of coarse equiaxed grains, which have a higher percentage of red and show a strong (001) orientation. After the addition of TiN particles, the microstructure of the S3 sample is mainly composed of fine equiaxed grains. The average grain sizes of S0 and S3 are 6.64 μm and 2.67 μm, respectively, indicating that the grains of the composite are significantly refined after the addition of TiN particles, which is consistent with the microstructure results observed by SEM. Furthermore, in addition, a decrease in the proportion of grains in red and an increase in the ratio of grains in blue and green are observed, indicating a weakening of the (001) orientation and an enhancement of the (111) and (101) directions.

Further analysis of the grain size distribution shows that after adding TiN particles, the size of large grains decreases more obviously, and the maximum grain size of composite materials does not exceed 10 μm. The effect of grain refinement is mainly caused by the following two reasons: (1) TiN produces a pinning effect at the grain boundaries and within the grains, thereby hindering the growth of grains; (2) TiN acts as an effective heterogeneous nucleation site during aluminum alloy solidification, which can strongly promote the nonuniform nucleation of melt and thus refine the grain [24].

As shown in Fig. 5(b) and (d), the volume fraction of the low-angle grain boundary (LAGB) increases from 18.3% to 22.6% [25]. An increase in LAGB indicates an increase in the density of dislocations. When the dislocation encounters obstacles during movement, the dislocation easily accumulates after being nailed, so the density of the dislocation continues to increase, making slip difficult to carry out and hindering the internal deformation of the

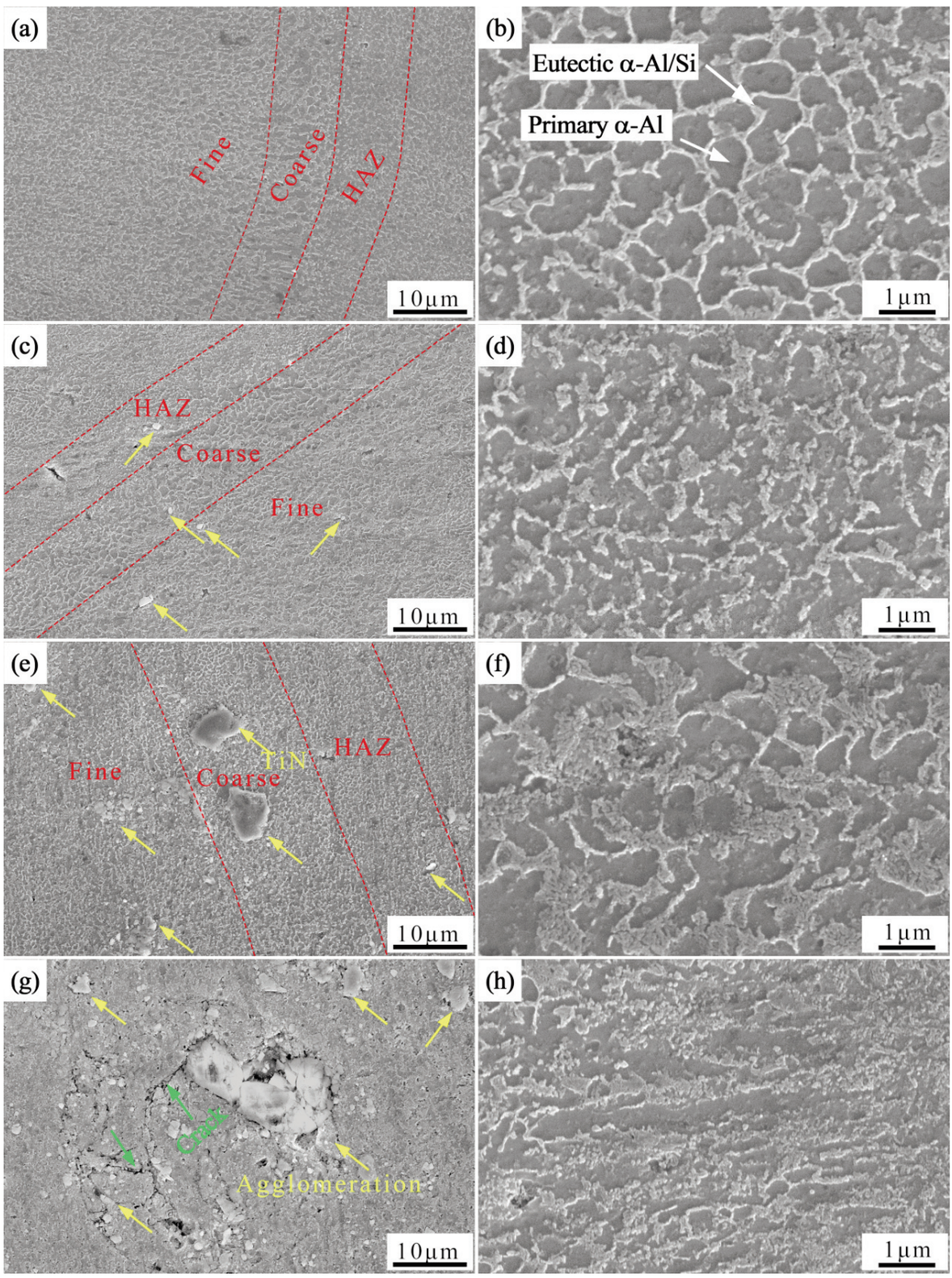

Figure 4. *SEM images showing the microstructures of the SLM samples with different TiN contents: (a) S0; (c) S1; (e) S3; (g) S5. (e-h) are the high-magnified SEM images of (a-g)*

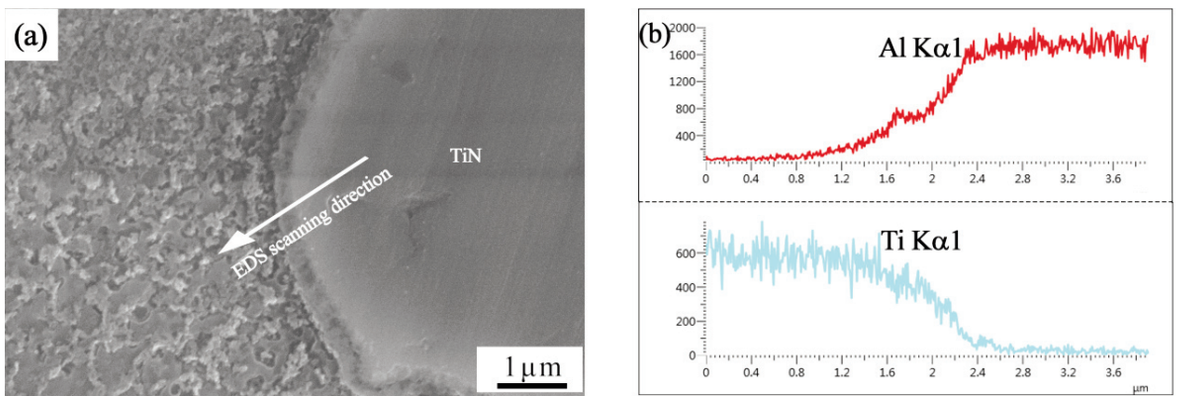

Figure 5. *Microstructure of unmelted TiN, and (b) distribution of Al and Ti elements along the EDS scanning direction*

material, resulting in increased strength. In addition, after the addition of TiN with low thermal conductivity, the heat transfer efficiency of the matrix decreases, and the rapidly changing thermal environment leads to the aggravation of local plastic deformation, forming more LAGBs [8].

According to the polar figure (PF) information, the texture index values of S0 (Fig. 6 (a)) and S3 (Fig. 6 (b)) are 5.19 and 2.42, respectively. This means that by adding TiN particles, the texture strength of the composites is weakened. Fig. 6(a) shows that the area with the highest intensity in the S0 polar diagram of the specimen is in the center of the polar diagram. The microstructure has a preferred orientation in the (001) direction; that is, the fiber texture appears on the longitudinal section of the building direction. Fig. 6(b) shows that there is no obvious preferred grain orientation of the SLM samples; instead, the grain orientation is randomly distributed.

3.4. Mechanical properties

3.4.1. Friction and wear properties

The coefficient of friction (COF) and wear rate of the AlSi10Mg and TiN/AlSi10Mg composites under a contact load of 3 N are shown in Fig. 7. As the TiN content increases, the wear resistance of the composites improves. The average COFs of S0, S1, S3 and S5 are 0.66, 0.62, 0.49, and 0.51, and the wear rates are 0.40, 0.31, 0.30, and 0.33 mm^3/h, respectively. Compared with that of the AlSi10Mg sample, the COF of S3 is reduced by 26%, and the wear amount is reduced by 33%. The friction coefficient curve of S5 is generally stable compared with that of the AlSi10Mg alloy. Since the hardness of the TiN particles is substantially higher than that of the aluminum matrix, there are several higher peaks in the friction coefficient results. Under the influence of compressive stress, numerous abrasive particles are forced into the friction surface repeatedly, causing the friction coefficient to cyclically increase. The results show that the addition of an appropriate amount of TiN particles can significantly improve the wear resistance of the alloy and change the wear mechanism. The high hardness and fine grain size of the TiN/AlSi10Mg composite material are the main reasons for the improved wear resistance. The significant increase in hardness indicates that the composite has good resistance to plastic deformation. On the other hand, the frictional heat generated in the process of the wear test results in the softening of the AlSi10Mg matrix, but the introduction of TiN particles can improve the high-temperature strength of the matrix and alleviate the wear effect of the matrix.

To investigate the influence of the TiN content on the wear mechanism of samples, the worn surface morphologies of S0, S1, S3, and S5 were observed, as shown in Fig. 8. The worn surfaces of the four samples display parallel grooves with some detached edges, indicating that microcutting-mode abrasive wear occurred during sliding wear. Adhesive wear has the characteristics of flaky spalling, large surface damage and high plastic deformation. The wear marks on the surface of the AlSi10Mg samples are deep and continuous along the sliding direction, while the wear marks on the TiN/AlSi10Mg composite are shallow and discontinuous along the groove. In the process of friction, severe plastic deformation and cyclic wear occur at the same time, which causes the soft AlSi10Mg to peel away from the worn surface and embed in the wear track as debris. The debris slides along the grinding ball and acts as a third body abrasive to produce microcuts, forming deep and long grooves on the worn surface. The physical properties of TiN particles and the matrix in the composites are very different, the lattice is discontinuous, and metallurgical bonding cannot be formed. The matrix falls off under cyclic shear stress and contact stress. When the particles are embedded in the surface of the sample, cracks occur in this area, and the cracks continue to extend under the drive of load stress, resulting in spalling pits, as shown in the figure.

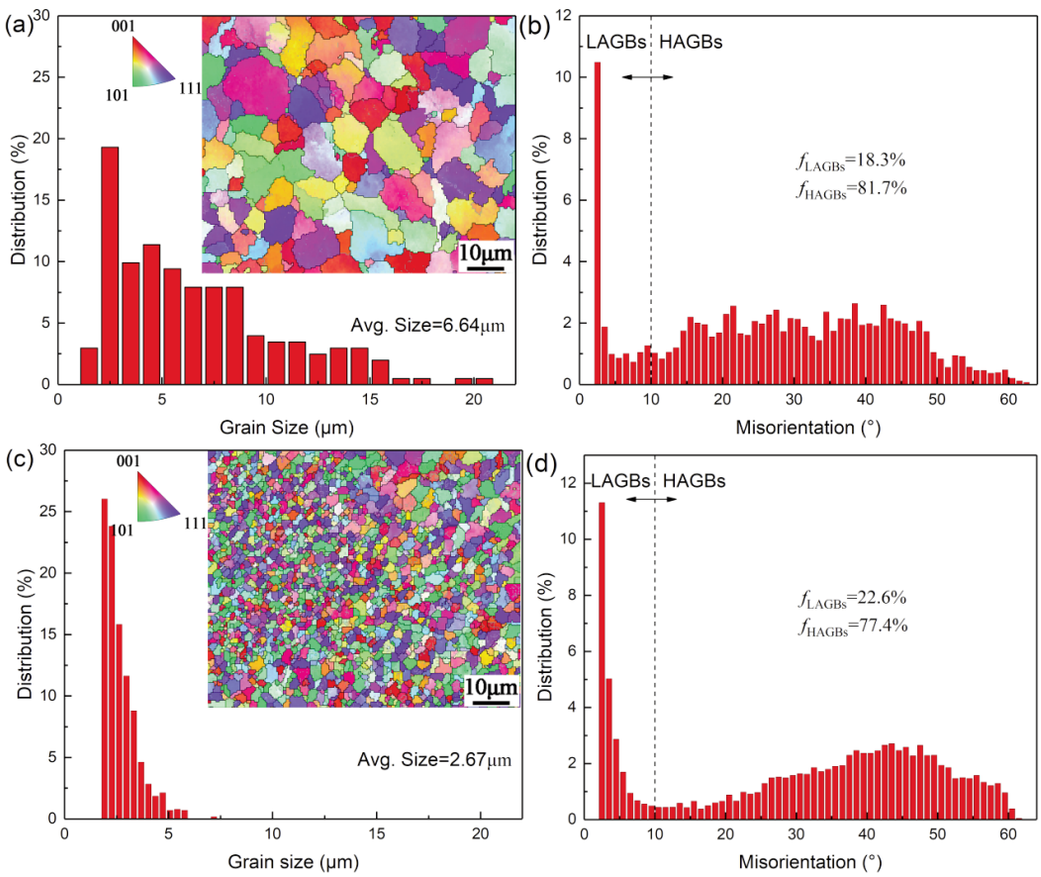

Figure 6. *EBSD results of the SLM AlSi10Mg and TiN/AlSi10Mg composites: (a) and (c) grain size distribution histograms of S0 and S3; (b) and (d) misorientation angle distribution maps of S0 and S3*

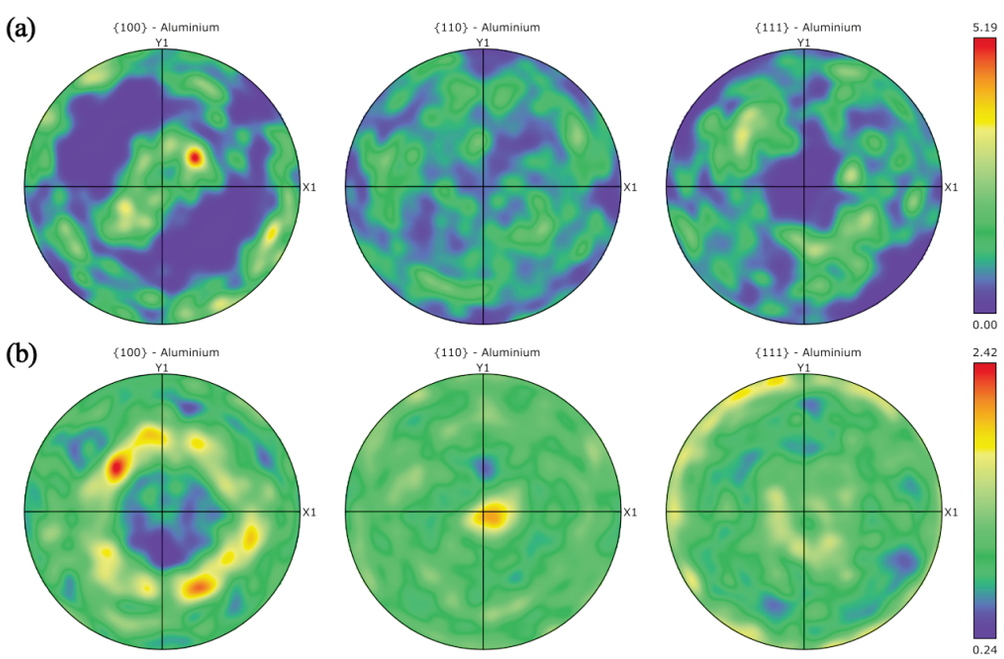

Figure 7. *EBSD pole figure maps of the SLM AlSi10Mg and TiN/AlSi10Mg composites: (a) S0; (b) S3*

Frictional heat is generated with the relative movement of the specimen and the grinding ball, and the Al in the specimen reacts with oxygen to form oxidation products, such as Al_2O_3 and SiO_2 [26], that is, the mechanical mixing layer (MML). The EDS results also confirm the presence of O elements in the worn area. The MML protects the matrix by preventing the friction pair from directly contacting the material surface [27-29]. It can be clearly seen that the surface of AlSi10Mg is severely worn by delamination, and the MML is peeled off under cyclic shear stress. However, the wear traces on the worn surface of TiN/AlSi10Mg composites are very shallow, and there is only a small amount of wear debris on the surface. The results show that the wear resistance of the TiN/AlSi10Mg composites is higher than that of AlSi10Mg. The improvement in the wear resistance of the TiN/AlSi10Mg composites can be attributed to the following two reasons. First, the presence of uniformly dispersed TiN particles in the composites hinders dislocation movement so that the surface strength of the matrix is higher and the corresponding wear resistance is better. Second, the frictional heat generated by the TiN/AlSi10Mg composites under a high load is conducive to the formation of a thick and stable MML, thereby reducing the contact between the grinding ball and the wear surface and reducing the wear rate of the material.

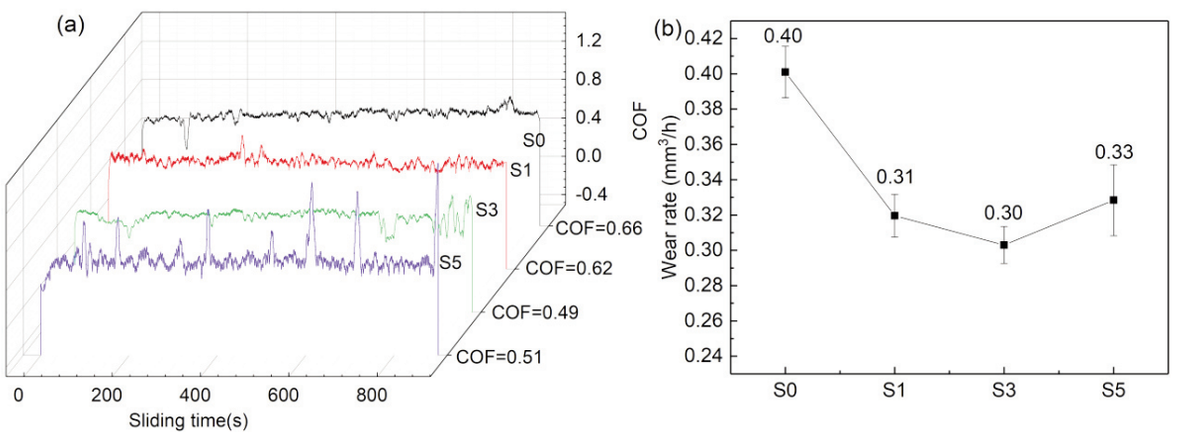

Figure 8. *Friction and wear properties of SLM AlSi10Mg and TiN/AlSi10Mg composite samples with different additions of TiN. (a) coefficient of friction; (b) wear rate*

3.4.2. Tensile properties and fracture behaviors

To determine the effect of the TiN content on the mechanical properties of the SLM TiN/AlSi10Mg composites, the Vickers hardness and tensile properties of samples S0, S1, S3, and S5 were tested, and the results are shown in Fig. 9 and Table 2. As shown in Fig. 9(a), the average hardness of S0 is 114.28 HV, and after the addition of TiN, the hardness of samples S1 and S3 increases to 116.46 HV and 132.36 HV, respectively, which are 1.9% and 15.52% higher than that of the unenhanced AlSi10Mg sample. With a further increase in TiN, the microhardness of the composites decreases to 124.14 HV. SLM layer-by-layer processing allows a material to achieve a nonequilibrium state of high frequency and rapid cyclic heating, which inhibits the precipitation of Si and results in solution strengthening. On the other hand, TiN is added to the AlSi10Mg matrix as a reinforcing phase to become a heterogeneous nucleation agent, and the grain size of the formed samples is gradually refined, resulting in fine-grain strengthening. According to the Hall–Petch formula, the strength of composites is directly related to the grain size, and the finer the grain size is, the higher the hardness value [30]. In addition, TiN particles are uniformly distributed in the matrix with the disturbance of the Marangoni flow during the fabrication process, resulting in dispersion strengthening and further improving the hardness of the material. The density of the sample also significantly affects the hardness of the material. When the TiN content is 5 wt.%, the defects caused by TiN agglomeration reduce the density of the sample and offset the strengthening effect caused by the TiN particles, reducing the hardness of sample S5.

Fig. 9(b) shows the tensile properties of the SLM AlSi10Mg and TiN/AlSi10Mg composites. Due to the compactness of the sample, the tensile strength of sample S1 decreases from 359.7 MPa to 296.7 MPa compared with that of AlSi10Mg. Due to the solution strengthening of Si and the significant fine-grain strengthening and dispersion strengthening of the TiN particles dispersed in the a-Al matrix [31], dislocation

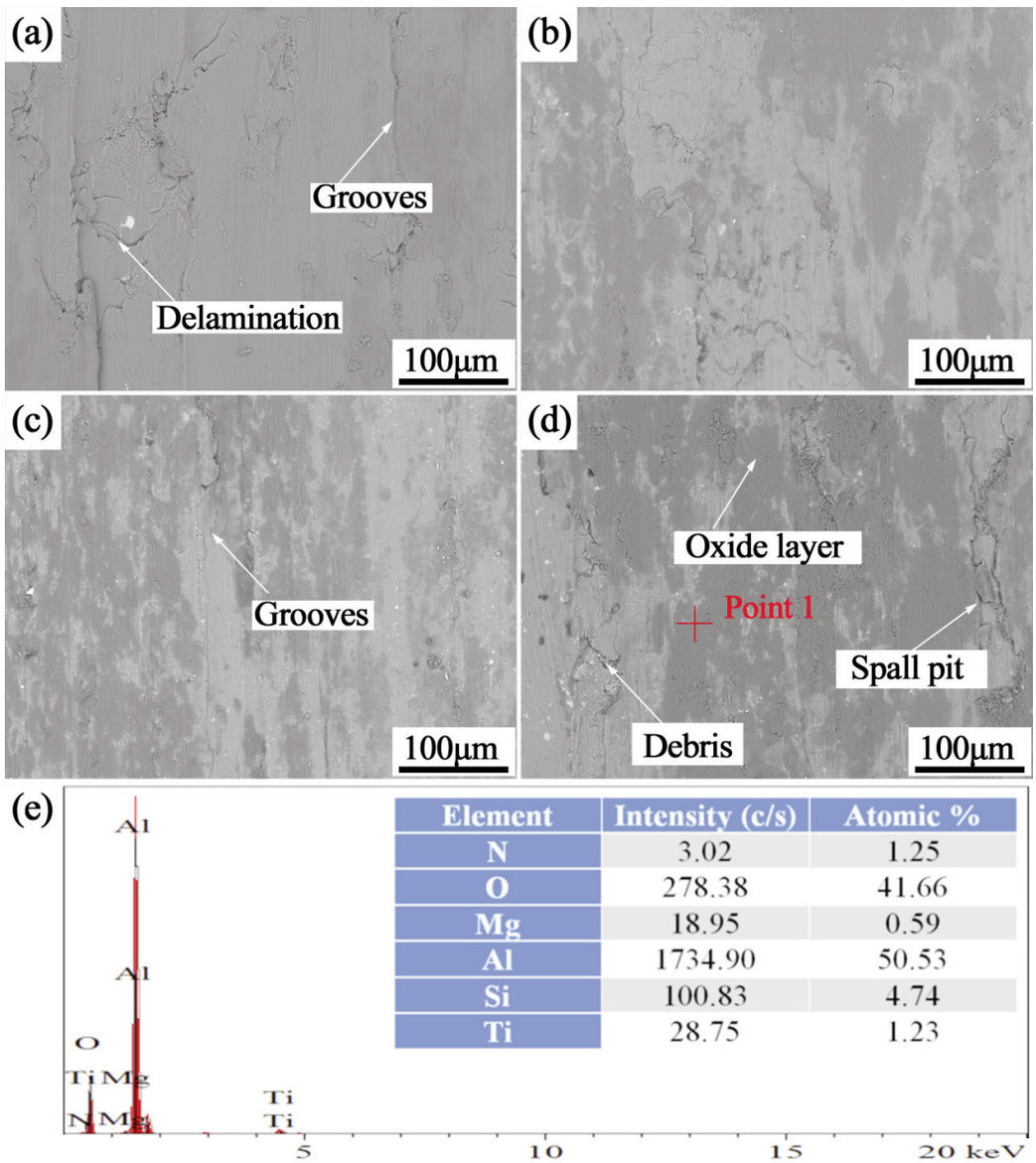

Element	Intensity (c/s)	Atomic %
N	3.02	1.25
O	278.38	41.66
Mg	18.95	0.59
Al	1734.90	50.53
Si	100.83	4.74
Ti	28.75	1.23

Figure 9. *SEM images showing the worn surfaces of the SLM samples. (a) S0; (b) S1; (c) S3; (d) S5; and (e) EDS result of point 1 in (d)*

Table 2. *Densification and mechanical properties of the SLM TiN/AlSi10Mg composite*

Specimen	UTS (MPa)	EL (%)	RD (%)	Hardness (HV)
S0	359.7 ± 14.4	8.1 ± 0.8	99.25	114.3 ± 4.4
S1	296.7 ± 10.5	8.3 ± 0.6	98.51	116.5 ± 3.9
S3	379.7 ± 4.6	13 ± 0.9	98.2	132.4 ± 4.1
S5	324.8 ± 13.6	5.1 ± 0.7	96.47	124.1 ± 5.4

and defect interactions in the plastic deformation process of the tensile samples hinder dislocation movement. The tensile strength of S3 peaks at 379.7 MPa, and the elongation shows the same upward trend, reaching 13.0%. In addition, those MP coarse and HAZ regions located at the boundary of the molten pool also have a certain influence on the tensile properties. Xiong [32] et al. claimed that the MPB was the weakest part of the SLM alloy. As the TiN content increases, the microstructure of the

molten pool boundary becomes more uniform. When the mass fraction of TiN reaches 3 wt.%, there is no obvious MP coarse or HAZ regions. The molten pool boundary can withstand the plastic deformation caused by the extension of the larger sample and improve the overall strength of the composite material. With a further increase in TiN content, the cracks caused by the agglomerated TiN particles are first destroyed during the stretching process and then rapidly expanded. Specifically, the tensile strength of S5 drops to 324.8 MPa, and the elongation also drops to 5.1%.

Fig. 10 shows the tensile fractography of S0, S1, S3, and S5. The macroscopic fracture morphologies of the SLM samples are shown in Fig. 10(a-d). The fracture surfaces of all specimens are rough and irregular, with obvious cracks and holes, and there is also obvious spheroidization for S0 and S5. Generally, small and round holes are caused by the pores present in the powder itself or by the protective gas trapped in the molten pool. The spheroidization phenomenon occurs during the SLM process, which is caused by excessive surface tension between the solid phase and the liquid phase due to the insufficient laser energy density in the local area of the molten pool. During the tensile tests, a large stress concentration is formed near the irregular pores, and the crack spreads rapidly along the crystal close-packed plane. The formation of a macroscopic failure zone results in the release of stress [33]. In the tensile fracture of S0, the cleavage platform characteristics of brittle fracture are observed, accompanied by tiny dimples, which belong to the mixed-mode of ductile and brittle fractures, and the brittle mode is given priority over the ductile mode. The fracture mode of the TiN/AlSi10Mg composite is similar to that of the AlSi10Mg material, but the difference lies in the larger number of dimples, the TiN particles present in the dimples, and the TiN clusters in the fracture. The large TiN particles or TiN clusters distributed at the grain boundaries of sample S5 were not melted during the SLM forming process and then remained in the matrix, and the brittle clusters acted as crack sources during the deformation process to reduce the strength and plasticity [10].

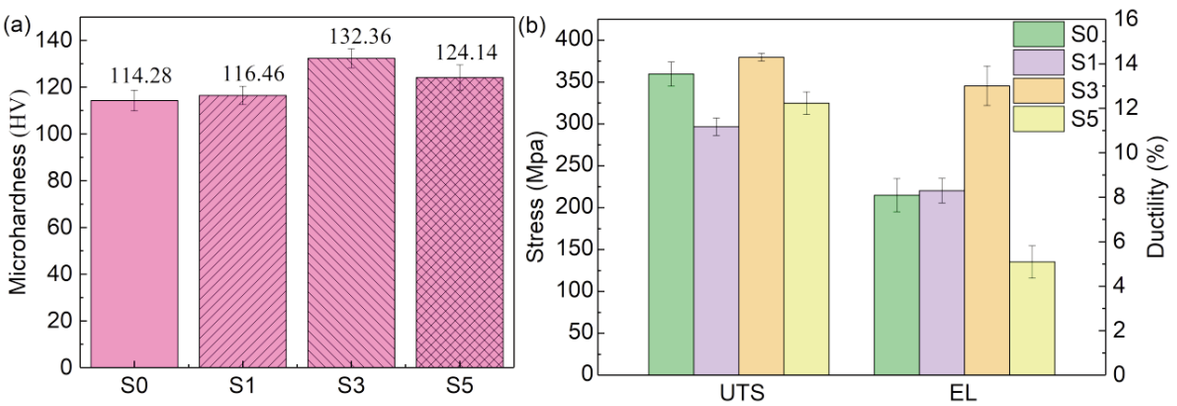

Figure 10. *(a) Microhardness and (b) ultimate tensile strength (UTS) and elongation (EL) of SLM samples with different TiN contents*

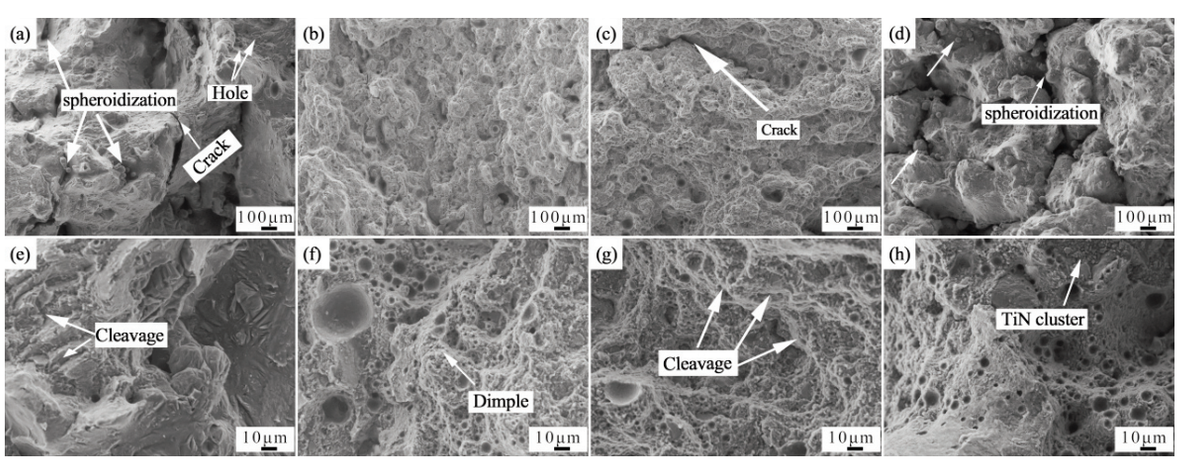

Figure 11. *SEM images showing the tensile fractography of the SLM TiN/AlSi10Mg composites with different TiN contents: (a) S0; (b) S1; (c) S3; (d) S5; (e-h) are magnified images of the fracture surfaces*

4. Conclusions

In this study, TiN ceramic-reinforced AlSi10Mg composites (AMCs) were produced through the SLM of TiN/AlSi10Mg composite powders. The effects of the TiN content on the densification behavior, microstructure evolution, crystal textures, and mechanical properties were investigated. The main conclusions are summarized as follows:

(1) The relative density of composite samples with 0–3 wt. % TiN is higher than 98% and further increasing the TiN content leads to a decrease in relative density. During SLM, TiN particles agglomerate and form defects, such as atmospheric pores and cracks.

(2) The addition of TiN has a significant effect on the microstructure. The microstructures of the AlSi10Mg and TiN/AlSi10Mg composite samples exhibit a primary a-Al matrix decorated with brilliant white eutectic Si networks. When the TiN content reaches 5 wt. %, the eutectic structure gradually changes from a network to thick sheets, and part of the network structure is broken. TiN acts as an effective heterogeneous nucleation site during the solidification of the aluminum alloy, strongly promoting the nonuniform nucleation of melt, significantly refining grain size, and weakening the texture in the (001) direction.

(3) The improved wear resistance of the TiN/AlSi10Mg composites can be attributed to two reasons. Firstly, the presence of uniformly dispersed TiN particles in the composites hinders dislocation movement resulting in a higher surface strength of the matrix and improved wear resistance. Secondly, the frictional heat generated by the TiN/AlSi10Mg composites under high load conditions promotes the formation of a thick and stable MML, reducing the contact between the grinding ball and the wear surface and reducing the wear rate of the material.

(4) The optimal addition amount of TiN is determined to be 3 wt. %. The optimized TiN/AlSi10Mg composites exhibit excellent mechanical performance (132.4±4.1 HV for hardness and 379.7± 4.6 MPa for tensile strength) with a low friction coefficient of 0.49. The enhanced strength is mainly attributed to the dispersion strengthening and the fine-grain strengthening.

Acknowledgements

This work was supported by the Fujian Industry University Cooperation Project (Grant No. 2020H6018), Fujian Innovation Center of Additive Manufacturing (Grant No. ZCZZ202-04, ZCZZ202-05). Natural Science Foundation Project of Fujian Province (Grant No. 2020J05179), and Science and Technology Project of Fujian University of Technology (Grant No. GY-Z20012).

Author Contributions

Weidong Huang: Conceptualization, Supervision, Methodology, Writing and editing, Lu Wang: Conceptualization, Writing-Original draft preparation, Investigation, Methodology, Data curation, Xu Huang: Supervision, Methodology, Funding acquisition, Resources, Dongdong He: Writing and editing, Xiaopeng Xu: Data curation, Xinxi Chen: Project administration, Xuheng Cheng: Software, Shuaishuai Qin: Translation and revision. Lihong Huang: Data curation

Conflicts of interest

The authors declare that they have no known competing financial interests or personal relationships that could have appeared to influence the work reported in this paper.

Data availability

The authors declare that the research data needed to support and reproduce the findings of this study are available within the article.

References

[1] J. L. Zhang, B. Song, Q. S. Wei, D. Bourell, Y. S. Shi, A review of selective laser melting of aluminum alloys: Processing, microstructure, property and developing trends, Journal of Materials Science & Technology, 35 (02) (2019) 270-284. https://doi.org/10.1016/j.jmst.2018.09.004.

[2] L. X. Xi, K. Ding, H. Zhang, D. D. Gu, In-situ synthesis of aluminum matrix nanocomposites by selective laser melting of carbon nanotubes modified Al-Mg-Sc-Zr alloys, Journal of Alloys and Compounds, (891) (2022) 891. https://doi.org/10.1016/J.JALLCOM.2021.162047.

[3] Q. H. Lu, Y. L. Ou, P. L. Zhang, H. Yan, Fatigue performance and material characteristics of SiC/AlSi10Mg composites by selective laser melting, Materials Science & Engineering A, 858 (2022) 144163. https://doi.org/10.1016/j.msea.2022.144163.

[4] L. Zhao, L. B. Song, J. G. S. Macías, Y. X. Zhu, M. S. Huang, A. Simar, Z. H. Li, Review on the correlation between microstructure and mechanical performance for laser powder bed fusion AlSi10Mg, Additive Manufacturing, 56 (2022) 102914. https://doi.org/10.1016/j.addma.2022.102914.

[5] X. Huang, Y. T. Zhu, W. D. Huang, S. S. Qin, L. Wang, Microstructure evolution and mechanical properties of TiB/Ti6Al4V composites based on selective laser melting, Journal of Mining and Metallurgy B: Metallurgy, 58 (3) (2022) 439-450. https://doi.org/10.2298/JMMB220422025H.

[6] Y. K. Xiao, H. Chen, Z. Y. Bian, T. T. Sun, H. Ding, Q. Yang, Y. Wu, Q. Lian, Z. Chen, H. W. Wang, Enhancing strength and ductility of AlSi10Mg fabricated by selective laser melting by TiB_2 nanoparticles, Journal

of Materials Science & Technology, 109 (2022) 254-266. https://doi.org/10.1016/j.jmst.2021.08.030.

[7] W. Cheng, Y. Z. Liu, X. J. Xiao, B. Huang, Z. G. Zhou, X. H. Liu, Microstructure and mechanical properties of a novel (TiB_2 +TiC)/AlSi10Mg composite prepared by selective laser melting, Materials Science and Engineering: A, 834 (2021) 142435. https://doi.org/10.1016/j.msea.2021.142435

[8] M. Wang, B. Song, Q. S. Wei, Y. S. Shi, Improved mechanical properties of AlSi7Mg/nano-SiCp composites fabricated by selective laser melting, Journal of Alloys and Compounds, 810 (2019) 151926. https://doi.org/10.1016/j.jallcom.2019.151926.

[9] N. K. Tolochko, Y. V. Khlopkov, S. E. Mozzharov, M. B. Ignatiev, T. Laoui, V. I. Titov, Absorptance of powder materials suitable for laser sintering, Rapid Prototyping Journal, (2000) https://doi.org/10.1108/13552540010337029.

[10] C. Gao, W. Wu, J. Shi, Z. Xiao, A. H. Akbarzadeh, Simultaneous enhancement of strength, ductility, and hardness of TiN/AlSi10Mg nanocomposites via selective laser melting, Additive Manufacturing, 34 (2020) 101378. https://doi.org/10.1016/lj.addma.2020.101378.

[11] X. P. Li, G. Ji, Z. Chen, A. Addad, Y. Wu, H. W. Wang, J. Vleugels, J. V. Humbeeck, J. P. Kruth, Selective laser melting of nano-TiB_2 decorated AlSi10Mg alloy with high fracture strength and ductility, Acta Materialia, 129 (2017) 183-193. https://doi.org/10.1016/j.actamat.2017.02.062.

[12] W. Li, U. Guler, N. Kinsey, G. V. Naik, A. Boltasseva, J. Guan, V. M. Shalaev, A. V. Kildishev, Refractory plasmonics with titanium nitride: broadband metamaterial absorber, Advanced Materials, 26 (47) (2014) 7959-7965. https://doi.org/10.1002/adma.201401874.

[13] C. Tan, J. Zou, D. Wang, W. Ma, K. Zhou, Duplex strengthening via SiC addition and in-situ precipitation in additively manufactured composite materials, Composites Part B: Engineering, 236 (2022) 109820. https://doi.org/10.1016/j.compositesb.2022.109820

[14] Y. J. Liu, S. J. Li, H. L. Wang, W. T. Hou, Y. L. Hao, R. Yang, T. B. Sercombe, L. C. Zhang, Microstructure, defects and mechanical behavior of beta-type titanium porous structures manufactured by electron beam melting and selective laser melting, Acta Materialia, 113 (2016) 56-67. https://doi.org/10.1016/j.actamat.2016.04.029.

[15] C. Zhao, N. D. Parab, X. X. Li, K. Fezzaa, W. D. Tan, A. D. Rollett, T. Sun, Critical instability at moving keyhole tip generates porosity in laser melting, Science, 370 (6520) (2020) 1080-1086. https://doi.org/10.1126/science.abd1587.

[16] L. X. Xi, S. Guo, D. D. Gu, M. Guo, K. J. Lin, Microstructure development, tribological property and underlying mechanism of laser additive manufactured submicro-TiB_2 reinforced Al-based composites, Journal of Alloys and Compounds, 819 (2020) 152980. https://doi.org/10.1016/j.jallcom.2019.152980.

[17] P. Mercelis, J. P. Kruth, Residual stresses in selective laser sintering and selective laser melting, Rapid prototyping journal, 12 (5) (2006) 254-265. https://doi.org/10.1108/13552540610707013.

[18] B. AlMangour, D. Grzesiak, J. M. Yang, Rapid fabrication of bulk-form TiB_2/316L stainless steel nanocomposites with novel reinforcement architecture and improved performance by selective laser melting, Journal of Alloys and Compounds, 680 (2016) 480-493. https://doi.org/10.1016/j.jallcom.2016.04.156.

[19] Q. Yan, B. Song, Y. S. Shi, Comparative study of performance comparison of AlSi10Mg alloy prepared by selective laser melting and casting, Journal of Materials Science & Technology, 41 (2020) 199-208. https://doi.org/10.1016/j.jmst.2019.08.049.

[20] Y. M. Chen, L. Z. Wang, Z. X. Feng, W. N. Zhang, Effects of heat treatment on microstructure and mechanical properties of SLMed Sc-modified AlSi10Mg alloy, Progress in Natural Science: Materials International, 31 (5) (2021) 714-721. https://doi.org/10.1016/j.pnsc.2021.08.003.

[21] B. Chen, S. K. Moon, X. Yao, G. Bi, J. Shen, J. Umeda, K. Kondoh, Strength and strain hardening of a selective laser melted AlSi10Mg alloy, Scripta Materialia, 141 (2017) 45-49. https://doi.org/10.1016/j.scriptamat.2017.07.025.

[22] Z. Feng, H. Tan, Y. B. Fang, X. Lin, W. D. Huang, Selective laser melting of TiB_2/AlSi10Mg composite: Processability, microstructure and fracture behavior, Journal of Materials Processing Technology, 299 (2022) 117386. http://dx.doi.org/10.1016/j.scriptamat.2017.07.025.

[23] Z. Y. Wang, L. C. Zhuo, E. H. Yin, Z. Zhao, Microstructure evolution and properties of nanoparticulate SiC modified AlSi10Mg alloys, Materials Science and Engineering: A, 808 (2021) 140864. https://doi.org/10.1016/j.msea.2021.140864

[24] S. Z. Zhang, Z. Chen, P. Wei, K. Huang, Y. T. Zou, S. Yao, M. Li, B. H. Lu, J. D. Xing, Microstructure and properties of a nano-ZrO_2-reinforced AlSi10Mg matrix composite prepared by selective laser melting, Materials Science & Engineering A, 838 (2022) https://doi.org/10.1016/j.msea.2022.142792.

[25] Y. W. Gui, Y. J. Cui, H. K. Bian, Q. N. Li, L. Ouyang, A. Chiba, Role of slip and {10-12} twin on the crystal plasticity in Mg-RE alloy during deformation process at room temperature, Journal of Materials Science & Technology, 80 (2021) 279-296. https://doi.org/10.1016/j.jmst.2021.01.006.

[26] K. Razavizadeh, T. Eyre, Oxidative wear of aluminium alloys, Wear, 79 (3) (1982) 325-333. https://doi.org/10.1016/0043-1648(82)90322-2.

[27] L. Y. Wu, Z. Y. Zhao, P. K. Bai, W. J. Zhao, Y. X. Li, M. J. Liang, H. H. Liao, P. C. Huo, J. Li, Wear resistance of graphene nano-platelets (GNPs) reinforced AlSi10Mg matrix composite prepared by SLM, Applied Surface Science, 503 (2020) 144156. https://doi.org/10.1016/j.apsusc.2019.144156.

[28] A. Riahi, A. Alpas, The role of tribo-layers on the sliding wear behavior of graphitic aluminum matrix composites, Wear, 251 (1-12) (2001) 1396-1407. https://doi.org/10.1016/S0043-1648(01)00796-7.

[29] J. Kováčik, Š. Emmer, J. Bielek, L. Keleši, Effect of composition on friction coefficient of Cu–graphite composites, Wear, 265 (3-4) (2008) 417-421. https://doi.org/10.1016/j.wear.2007.11.012.

[30] D. D. He, H. Wang, W. D. Huang, X. X. Chen, G. F. Lian, Y. Wang, Microstructure and mechanical properties of LaB_6/Ti-6Al-4V composites fabricated by selective laser melting, Metals, 13 (2) (2023) 264. https://doi.org/10.3390/met13020264.

[31] J. Hou, W. Chen, Z. E. Chen, K. Zhang, A. J. Huang,

Microstructure, tensile properties and mechanical anisotropy of selective laser melted 304L stainless steel, Journal of Materials Science & Technology, 48 (2020) 63-71. https://doi.org/10.1016/j.jmst.2020.01.011.

[32] Z. H. Xiong, S. L. Liu, S. F. Li, Y. Shi, Y. F. Yang, R. D. K. Misra, Role of melt pool boundary condition in determining the mechanical properties of selective laser melting AlSi10Mg alloy, Materials Science and Engineering: A, 740 (2019) 148-156. https://doi.org/10.1016/j.msea.2018.10.083.

[33] Y. M. Xiao, Y. Q. Yang, S. B. Wu, J. Chen, D. Wang, C. H. Song, Microstructure and mechanical properties of AlSi10Mg alloy manufactured by laser powder bed fusion under nitrogen and argon atmosphere, Acta Metallurgica Sinica, 35 (3) (2022) 486-500. https://doi.org/10.1007/s40195-021-01354-7.

RAZVOJ MIKROSTRUKTURE, MEHANIČKA SVOJSTVA I OSNOVNI MEHANIZAM AlSi10Mg KOMPOZITA OJAČANIH MIKRO TiN PROIZVEDENIH SELEKTIVNIM LASERSKIM TOPLJENJEM

X. Huang [a, b], L. Wang [b], W.-D. Huang [a, b, *], D.-D. He [b], X.-H. Cheng [b], X.-P. Xu [b], X.-X. Chen [b], S.-S Qin [a, b], L.-H. Huang [a, b]

[a] Ključna laboratorija za inteligentnu tehnologiju i opremu za obradu u Fudžijanu, Univerzitet tehnologije u Fudžijanu, Fužou, Kina

[b] Fakultet za mehaničko i automobilsko inženjerstvo, Univerzitet tehnologije u Fudžijanu, Fužou, Kina

Apstrakt

U ovoj studiji, kompoziti sa aluminijumskom matricom ojačani sa TiN izrađeni su primenom tehnike selektivnog laserskog topljenja (SLM). Studija istražuje efekte sadržaja TiN na gustinu, razvoj mikrostrukture, kristalne teksture i mehanička svojstva. Rezultati pokazuju da relativna gustina uzoraka kompozita koji sadrže 0-3% TiN prelazi 98%. Međutim, dalje povećanje sadržaja TiN dovodi do smanjenja relativne gustine. Čestice TiN pokazuju ravnomernu raspodelu i efikasnu kvašljivost sa matricom AlSi10Mg, uz formiranje slojevite međufaze. Čestice TiN vrše rafinaciju zrna matrice i značajno smanjuju prevalenciju preferirane teksture (001) promovišući heterogenu nukleaciju. U poređenju sa legurom AlSi10Mg, kompozit TiN/AlSi10Mg pokazuje poboljšanu mikrotvrdoću, čvrstoću na pritisak i otpornost na habanje. Izuzetna mehanička svojstva kompozita aluminijumske matrice se pripisuju efektu disperzionog ojačavanja česticama TiN i ojačavanju granicama zrna matrice. Optimalan sadržaj TiN određen je kao 3%, što rezultuje izuzetnim mehaničkim performansama izrađenih uzoraka (132.4±4.1 HV za tvrdoću i 379.7±4.6 MPa za zateznu čvrstoću) uz nizak koeficijent trenja od 0.49.

Ključne reči: *Selektivno lasersko topljenje; TiN/AlSi10Mg kompoziti; Razvoj mikrostrukture; Mehanička svojstva*